

# The Sixth UltraVISTA Data Release

## The Legacy Release

A. Moneti, H. J. McCracken, S. Rouberol,  
(Institut d’Astrophysique de Paris);  
J. Dunlop, M. Franx, J. Fynbo, R. Bowler, B. Milvang-Jensen (UltraVISTA);  
C. Gonzalez-Fernandez, E. Gonzalez-Solares, J. Irwin, M. Irwin (CASU);  
R. Blake, N. Cross, R. Mann, M. Read, E. Sutorius (WFAU).

May 27, 2024

**Data Collection:** UltraVISTA  
**Release number** 6  
**Data provider:** Jim Dunlop  
**Date:** May 27, 2024

## 1 Abstract

UltraVISTA (McCracken et al. 2012) is an ultra-deep near-infrared survey of the central  $1.5^\circ \times 1.2^\circ$  region of the COSMOS field (Scoville et al. 2007) using the VIRCAM instrument on the VISTA telescope. The observations began in December 2009 and finished in March 2023 when the instrument was decommissioned. This document describes the sixth and last UltraVISTA data release, “DR6” or “Legacy”, which comprises stacked images and catalogues in  $YJHK_s$  and the NB118 narrow-band filter. The observations obtained since the DR5 release were mostly in the Y-band “deep” stripes in order to bring them to the same depth as the previously observed “ultra-deep” stripes. Thus, in this release, the depth is nearly uniform over the full field for the broad-band  $YJHK_s$  filters. This release also uses the GTO data (Milvang-Jensen et al. 2013) obtained in 2010 in the  $J$  and the NB118 filters in the “deep” stripes.

### 1.1 Acknowledging these data products

Any publications using these data products must include this text:

**“Based on observations collected at the European Southern Observatory under ESO programmes 179.A-2005, 198.A-2003, 1104.A-0643, 110.25A2 and 284.A-5026 and on data obtained from the ESO Science Archive Facility with DOI <https://doi.org/10.18727/archive/52>, and on data products produced by CANDIDE and the Cambridge Astronomy Survey Unit on behalf of the UltraVISTA consortium.”**

In addition, a reference to the UltraVISTA DR1 survey paper should be included: McCracken et al. (2012). And if you use the NB118 data, the reference Milvang-Jensen et al. (2013) should also be added.

## 2 Overview

The DR6 release was built from all UltraVISTA data ever taken, from the start of the survey in December 2009 to the decommissioning of VIRCAM in March 2023. Additionally, the data from the NB118 GTO programme (Milvang-Jensen et al. 2013) were included in DR6, thereby providing coverage over the full UltraVISTA field also in NB118, albeit at a varying depth (see Fig. 13). The five ESO programmes used to make DR6 are listed in Tab. 1. For a recent overview of UltraVISTA, see Dunlop et al. (2023).

ProgID	Type	PI(s)	Alloc.	Filter(s)	Obs.	DR(s)
179.A-2005	PS	Dunlop, Le Fèvre, Franx, Fynbo	1800 h	YJHKN	2009–2018	DR1–DR6
198.A-2003	PS	Dunlop	756 h	JHK	2017–2022	DR5–DR6
1104.A-0643	LP	Dunlop	272 h	Y	2019–2022	DR6
110.25A2	DDT	Milvang-Jensen	100 h	JHK	2023	DR6
284.A-5026	GTO	Fynbo	30 h	JN	2010	DR6

**Table 1:** ESO programmes contributing to the UltraVISTA DR6. For *Type*, the abbreviations are: PS = Public Survey, LP = Large Programme, DDT = Director’s Discretionary Time, and GTO = Guaranteed Time observations. For *Filter(s)*, K means  $K_s$  and N means NB118.

The VIRCAM footprint on the sky (the so-called pawprint) consists of 16 widely spaced detector images, as shown in Fig. 1(left). By stepping up and down a set of four stripes is covered, and by moving in the other direction a full so-called tile is covered. UltraVISTA used this to define the four *deep stripes* and the four *ultra-deep stripes* shown in Fig. 1(right).

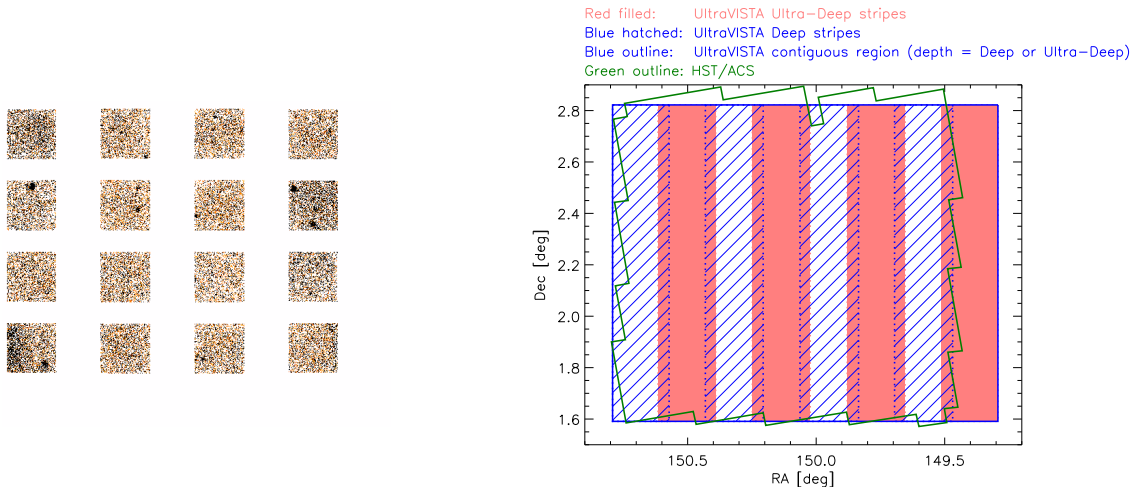


**Figure 1:** **Left:** The VIRCAM pawprint consisting of 16 widely spaced detectors covering a total of  $0.6 \text{ deg}^2$  (adapted from Milvang-Jensen et al. 2013). **Right:** The UltraVISTA field of  $1.5^\circ \times 1.2^\circ = 1.8 \text{ deg}^2$  comprised of four *deep stripes* (blue hatched) and four *ultra-deep stripes* (red filled) (from McCracken et al. 2012). The stripe layout comes from stepping the pawprint up and down.

Figure 2 shows the number of files obtained per month (approximate, as the years were divided in 12 equal months for the purposes of the figure), with different colours for the deep and ultra-deep stripes. As can be seen, the observing time was first mainly spent on the *ultra-deep stripes*,

and then later on the *deep stripes*. Here in DR6 at the end of the survey, the depth is essentially the same over the full field in the four broad-band filters, as described in Sect. 4.4.3.

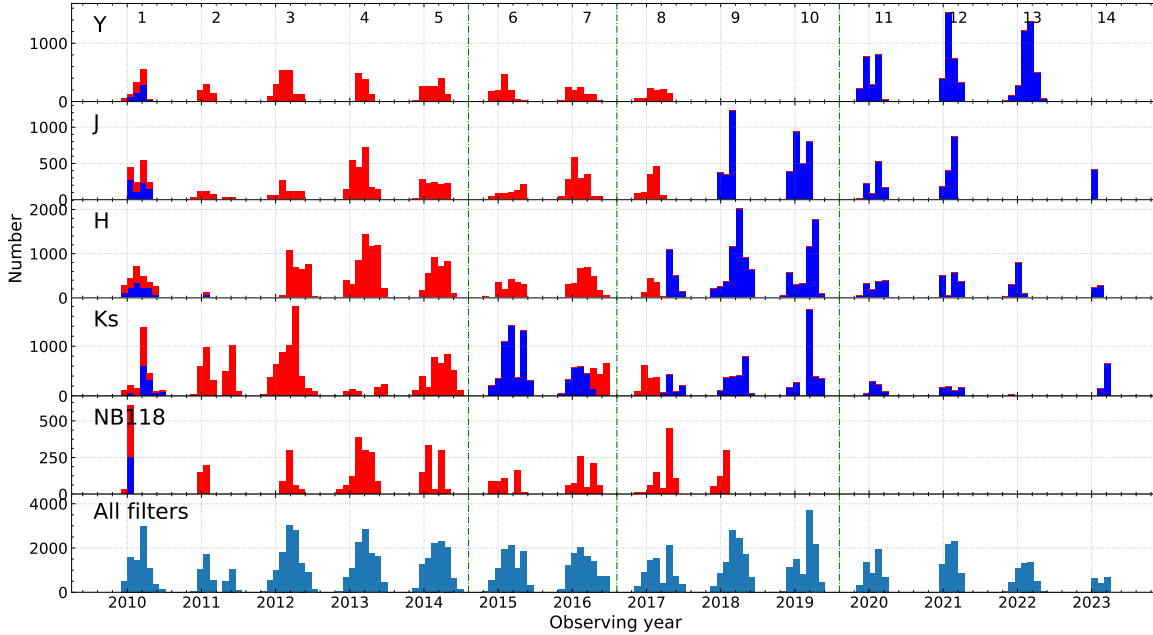


**Figure 2:** Observations per month for each filter; red are the ultra-deep stripes observed first, blue are the deep stripes observed later. The season number is indicated on the top panel, where an observing season typically goes from mid November to end June. The ends of the periods used for the DR3, DR4 and DR5 releases are indicated by the green dashed lines. DR6 covers the full time span of this figure. The figure shows the number of files — the exposure time per file is as follows:  $Y$  and  $J$ : 2 min,  $H$  and  $K_s$  1 min, and NB118 ca. 5 min in season 1, and 2 min thereafter. Note that this figure is for all the data obtained thus including the  $\sim 10\%$  of files that were later rejected as described in Section 4.

As in the previous releases, we begin with the data pre-processed by CASU<sup>1</sup> (Cambridge Astronomy Survey Unit), who performed dark subtraction, flat-fielding, non-linearity correction, gain normalisation, and an initial sky subtraction (e.g. Irwin et al. 2004; Lewis et al. 2010, and the CASU web site<sup>2</sup>). A total of 110,443 individual images and their ancillary files (flat fields, sky frames, stacks) were downloaded from the CASU website and processed as described below. Of these, 99,845 images passed our selection criteria (mainly on PSF FWHM and ellipticity, cf. Fig. 3) and were used to produce the stacks in the five filters.

The main purpose of our reprocessing is to improve the sky subtraction, as will be described below, and to produce stacks of all selected files. The overall workflow changed little from DR5, the main changes being in the selection of the frames to reject (details below) which resulted in fewer files being rejected. The “global” object mask, used to produce individual masks to avoid faint sources when building the individual skies, was built from the DR5 stacks except for the NB118 “deep” stripes, for which there was no prior data, and which was built from a stack of the CASU files. The *Gaia* EDR3 reference catalogue (Gaia Collaboration et al. 2016, 2021; Lindegren et al. 2021) was used for the astrometric calibration, and updated versions of the Astromatic<sup>3</sup> codes are used in the processing.

<sup>1</sup><http://casu.ast.cam.ac.uk>

<sup>2</sup><http://casu.ast.cam.ac.uk/surveys-projects/vista/technical/data-processing>

<sup>3</sup><https://www.astromatic.net/>

## 3 Release Content

### 3.1 Overview

In this release we provide five stacked images and their corresponding weight maps for  $YJHK_s$  and NB118<sup>4</sup> narrow-band data taken during all 14 years of UltraVISTA survey operations; the new data mainly add exposure time to the “deep” stripes in the  $Y$  band to bring them to the same depth as the “ultra-deep” stripes. Also, in DR6 we have added the GTO data (Milvang-Jensen et al. 2013), which provide NB118 coverage in the “deep” stripes which was absent before. In addition, single band individual source lists and source lists created in dual-image mode (using the  $K_s$  image as a detection image) are provided (note that in ESO terminology, single-band tabular data are referred to as “source lists” and multi-band merged data are referred to as catalogues). We also provide a five-band catalogue that meets the requirement for a catalogue in the Phase 3 framework. The data volume is  $\sim 90$  GB as in DR5.

The total survey area is close to  $1.9 \text{ deg}^2$ . Note that, as in DR4 and DR5, the “bad” region of detector 16 (having an unstable QE and higher noise) has not been masked. The noise maps in Figs. 9–13 show this effect in the lower left (where detector 16 is found when N is up and E is left) — note that the higher noise is mainly visible in the blue bands ( $Y$ , NB118 and  $J$ ).

### 3.2 Special image header contents

The files released follow ESO’s Phase 3 standard for the FITS headers, including the type and form of the provided metadata. As previously, we have made a small extension to this scheme in the form of COMMENT FITS header cards to provide additional information related to the stripe layout of UltraVISTA (Fig. 1). This was more relevant in earlier releases, where the depth was different in the two sets of stripes — in DR6 that is only the case in NB118<sup>5</sup>. Specifically, we have set the EXPTIME keyword (giving the typical exposure time per pixel in seconds), to the value for the ultra-deep stripes. And in COMMENT lines we list the value for both sets of stripes, e.g. for the  $H$ -band stack:

```
COMMENT ultra-deep stripes: typ. exptime per px = 690160.0 s (keyword EXPTIME)
COMMENT      deep stripes: typ. exptime per px = 630320.0 s
```

Similarly we have set the ABMAGLIM keyword (giving the limiting magnitude) to the value for the ultra-deep stripes, and given the value for both sets of stripes in COMMENT lines, e.g. for the  $Y$ -band stack:

```
COMMENT ultra-deep stripes: typical ABMAGLIM = 25.7 (keyword ABMAGLIM)
COMMENT      deep stripes: typical ABMAGLIM = 25.7
```

Finally, we follow the standard and provide keywords DIT and NDIT keywords only in the stacks where all the individual images had the same value of DIT and/or NDIT. In all stacks we give the breakdown of number of individual images on the different DIT,NDIT combinations in COMMENT lines, e.g. for the  $Y$ -band stack:

---

<sup>4</sup>The 16 NB118 filters (one per detector) are described in Milvang-Jensen et al. (2013)

<sup>5</sup>The noise (depth) over the field will be shown later in Figs. 9–13; this is also encoded in the included weight map images with pixel values proportional to the inverse variance.

```

COMMENT Breakdown of the used images on different N_DIT,DIT combinations
COMMENT N_images N_DIT DIT
COMMENT      992    4   30
COMMENT     14812   2   60

```

## 4 Data processing

All processing was performed on CANDIDE (Computer for Deep Imaging Data for Euclid) cluster of the CALET<sup>6</sup> (Collaboration for wide-field Astronomy Linked to Euclid and other Telescopes) data centre. As the name suggests, this data centre is primarily dedicated to processing associated ground- and space-based data for Euclid and the Euclid calibration fields including UltraVISTA/COSMOS. This structure ensures that we have support for processing operations well after the completion of UltraVISTA.

The post-DR5 data, covering the period from Nov 2019 to Mar 2023, were downloaded from the CASU web site. As before, these data include the individual sky-subtracted images, the corresponding sky frames (typically one sky frame for each CASU stack covering 0.5–1 h exposure), flat-fields, bad pixel maps and stacked `_st` images. The CASU data are arranged in OBs (Observation Blocks) of typically 15 or 30 image files (@ 2 min exposure) for  $Y$ ,  $J$  and NB118 and 30 or 60 files (@ 1 min exposure) for  $H$  and  $K_s$  (but sometimes just a few files), obtained with the same filter and dithered around one of the “paw” positions. The CASU processing builds a sky image from each OB and subtracts it from each file of the OB. Then the mean value of the subtracted sky is added back to the image in order to keep noise properties correct.

### 4.1 Pre-processing, astrometric and photometric calibration, and initial selection

As in previous releases, the processing begins with an image characterisation step in which the PSF’s FWHM and ellipticity  $e$  are determined for each extension of each image file using a dedicated run of `SExtractor` followed by `PSFEx` (Bertin 2011). Regarding the FWHM and ellipticity determination, it is important to note that the results depend on the stars selected, which is determined by the `DETECT_THRESHOLD` and the `SATUR_LEVEL` parameters of `SExtractor`. In DR4 we used 20/35000; in DR5, in an attempt to be more selective by choosing only brighter sources, and more conservative on the saturation side, we used 50/25000. But it turns out that the DR5 values were much too stringent so there were generally fewer valid stars than in DR4, and in some cases none at all, as when the background level was very high. So for DR6 we lowered the `DETECT_THRESHOLD` to 5 and raised the `SATUR_LEVEL` to 30000 to ensure a good number of valid stars. Also, since the selection is done at file level, not at chip level, the values for the file were computed as the mean non-zero chip values.

Figure 3 shows the seeing and ellipticity distributions, measured on all the images, separated by filter. The red solid line represents an estimate of the mode of each distribution, and the blue dashed line shows the cut-off thresholds adopted (FWHM > 1.0'' or  $e > 0.1$ , as in previous releases).

---

<sup>6</sup><https://calet.org/calet/>

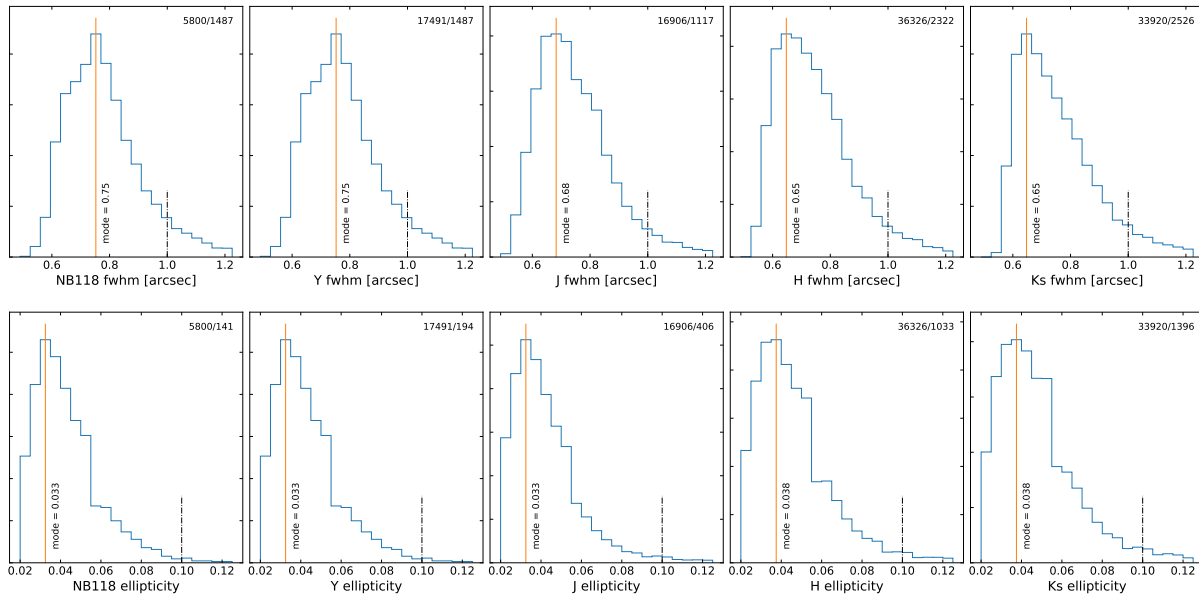


**Figure 3:** PSF FWHM (top) and ellipticity (bottom) distributions for all images considered for DR6. The orange solid line indicates the mode of each distribution. The blue dashed line shows the cut-off thresholds adopted: images with worse PSF than this were not used to make the DR6 stacks.

**Scamp** was used to determine the astrometric correction. Given the large number of files, it is impractical to process them all in a single run, so the files were grouped first by season (each season going from November to May) and then again, if needed, into smaller groups of up to 2000 files each. Also, for each season we determined the mean epoch of observations ( $0.16 \pm 0.04$  fractional years from the beginning of each year, i.e.  $\sim 28$  February  $\pm 14$  days), all filters combined, and used season-specific reference catalogues built by shifting the reference coordinates to those epochs using the *Gaia* proper motions.

The **Scamp** contrast factor was then used to perform a pre-selection that replaced the selection criterion based on the width of the histogram of valid pixels used in DR5. The distribution of these contrasts, for each filter, are shown in Figure 4. A detailed check of files with values lower than the bulk showed that they have significant problems: For the *H* band we examined manually all the 80 files with contrast  $< 62$ . Nearly all show one of the following problems:

1. very bright sky background, which results in few stars begin measurable, among other problems;
2. large PSF (typically FWHM larger than  $5''$ );
3. some or all of chips 9–16 showing abnormally high noise or other electronics-like problem (the histogram method devised for DR5 was used to identify files with this problem);
4. obvious tracking problems, like trails or double images;

Most of the low-contrast files were classified B, C or R by ESO, or were left unclassified, though some were still classified A. Visual inspection of a few that were classified A mostly showed telescope tracking problems. In conclusion it was decided to reject all files with low **Scamp** contrast before further processing.

In addition to determining the astrometric correction, here based on the *Gaia* EDR3 catalogue, **Scamp** also performs a photometric calibration. While for the astrometric correction each file

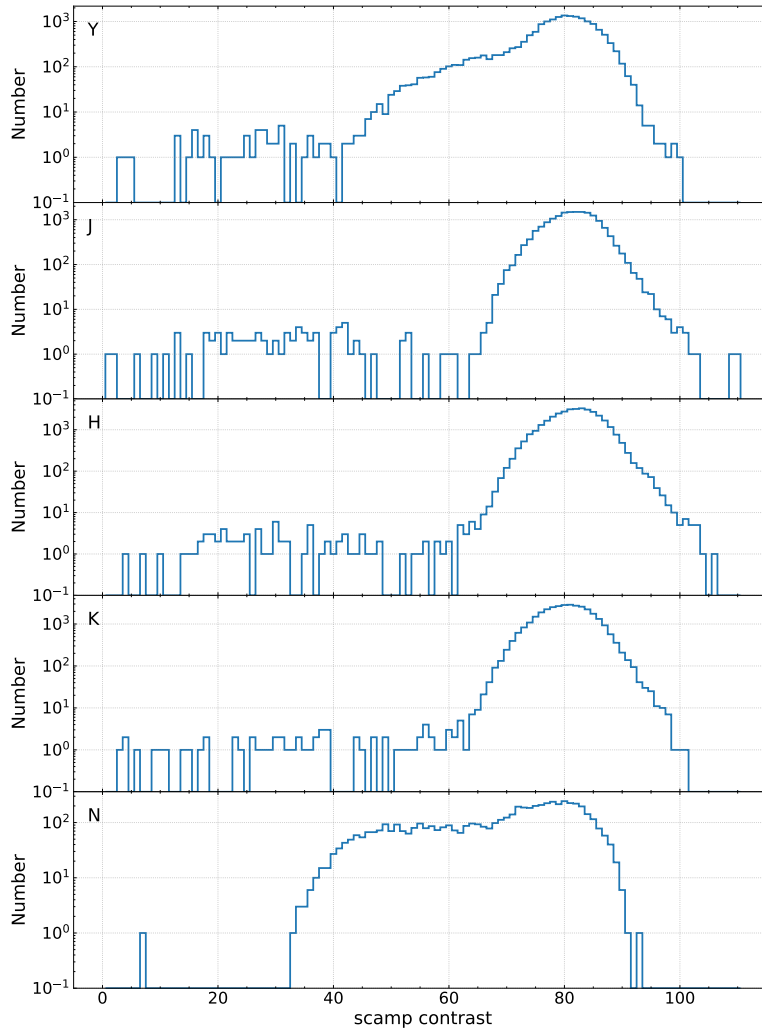


**Figure 4:** Distribution of Scamp contrast values.

can be processed individually, for the photometric correction they must be processed together and a reference file must be established. By default **Scamp** uses the first file of each group as a photometric reference, and the **FLXSCALE** keyword of all subsequent files are adjusted to be consistent with that file. But as the processing was split into multiple groups, this would have yielded a different calibration among the different groups. But **Scamp** also offers a method of declaring which file or files to use as photometric reference (in practice this is done setting a setting the **PHOTREF** keyword of the file). Our solution was to select all files with FWHM close to the median value as photometric reference files, which ensures that many such files are found in each group. While this is not a guarantee that the identical reference value is used in all groups, it should ensure a good level of homogeneity. The selection is then based on the **ZPcorr** (zero-point correction) parameter produced by **Scamp**. Typically the correction is  $< 0.1$  mag, but in some cases it was much larger. Visual inspection shows that this occurred in conjunction with tracking problems or in parallel with a rapidly rising sky, suggesting the arrival of clouds. In the end files with a photometric correction factor  $> 0.5$  mag were rejected before further processing, which accounts for 56 files, all filters combined.

In DR5 we also rejected a few hundred files for which `Scamp` gave an astrometric correction larger than  $\sim 30''$ . These files looked fine on visual inspection, and this problem was not understood at the time, but the files were nevertheless rejected to remain on the safe side and to avoid unexpected problems. Upon further study, it was found the coordinates in the file headers were incorrect (in many cases a problem file had the same coordinates as the previous one in the list) and that `Scamp` was correct in its correction determination, so this rejection criterion was removed in DR6.

Note that while in DR5 the rejected files were still used for sky building, but then excluded when building the stacks, here the few files with low `Scamp` contrast or large ZP correction were rejected at this level already. Then, as in DR5, the files large or elongated PSF were retained for sky building and excluded only at the stacking level.

## 4.2 Building individual skies

While early releases used a *first pass* stack of valid images to produce a *global* mask of objects, in DR5 and now in DR6 this mask was built from the final products of the previous release. There is one exception here: for the deep stripes of the NB118 filter which, while observed in 2010 in the GTO run (Milvang-Jensen et al. 2013), were not part of the regular survey and were not included in the previous releases. Thus a first pass stack, i.e., a stack of the CASU files, was built for them.

These masks, one per filter, are used to build *local* masks for each input file that include objects much fainter that could be identified in the individual files themselves.

Prior to determining the sky for each image, the originally subtracted CASU sky is added back in and the constant sky (as given in the `SKYLEVEL` keyword) removed. Then, for each *source* image a sky frame is built from a minimum of 4 and up to 20 other images obtained within 20 min of the *source* image. These images are masked with the source mask derived from the global mask as described above, then normalised to the value of the sky of the *source* file, and finally median (stack) filtered to produce a source-free image of the sky. This sky image is then subtracted from the *source* image.

All filters considered,  $\sim 76\%$  of the sky files are built with 20 files,  $\sim 22\%$  are built with between 14 and 19 files, and the remaining just under 2% are built with 13 files or less. Finally there are only 43 files without the minimum of 4 nearby images to build a sky frame, and thus they were rejected. These were typically files from executions of OBs that were quickly aborted, and thus were typically of dubious quality anyway. Also, each pixel of a sky frame built from 20 files used typically 15 of the files, the other 5 having that pixel masked. There are typically  $\sim 2\%$  of the pixels for which none of the pixels in the files used to build the sky are valid, mostly coming from the large regions masked around the bright stars. These are flagged in the sky-subtracted frame by setting their weight to nought.

Finally, a destriping (in both  $x$ - and  $y$ - directions) operation and the removal of any residual large-scale gradient was performed on each file in the same manner as in DR5. These *cleaned* files were then co-added to produce the final products.



### 4.3 Building the final stacks

It is at this stage, just prior to co-addition (stacking), that file rejection is applied according to the criteria on FWHM and ellipticity described earlier.

Co-addition is performed using *Swrap* (Bertin et al. 2002). As in the case of *Scamp* it is impractical to process all files in a single run of *Swrap*. We thus split the full list by paw, then again by season, and then further, if necessary, into similar size groups of less than  $\sim 500$  files. For each group the images and weight maps are combined using the *clipped mean stacking* outlier removal technique described in Gruen et al. (2014) with `CLIP_SIGMA = 4.0` in order to build an image substack and its weight map as implemented in *Swrap*. These are built onto the standard COSMOS pixel grid, the same as used previously, with  $0.15''$  per pixel. Finally, the substacks are merged using a simple weighted average to produce the final full stacks.

### 4.4 Data quality

#### 4.4.1 Astrometric accuracy

The overall astrometric accuracy was measured on the final stacks using catalogues extracted from the stacks and matching them to the *Gaia* EDR3 reference catalogue. In principle the reference catalogue should be shifted to the mean epoch of the data, but the mean epoch of all the data (all filters) combined is 2015.90, which is so close to the epoch of the EDR3 catalogue (2016.0), that we ignored that shift (but recall, as seen in Section 4.1, that catalogues shifted to the mean epoch of each season were used in the determination of the astrometric solution of the  $\sim 100,000$  individual images before stacking them). In addition, for each final stack, the mean epoch depends on when the observations in that filter were obtained, which differs between the ultra-deep and deep stripes (see Figs. 1 and 2); more on this towards the end of this section.

Figure 5 shows the difference between the measured and the reference RA and Dec for all filters. Each plot is roughly the size of an instrumental pixel (0.34 arcsec), and the red box is the size of the stack pixel (0.15 arcsec). And Table 2 lists the mean and FWHM of those distributions, which are about 1/3 of a instrumental pixel.

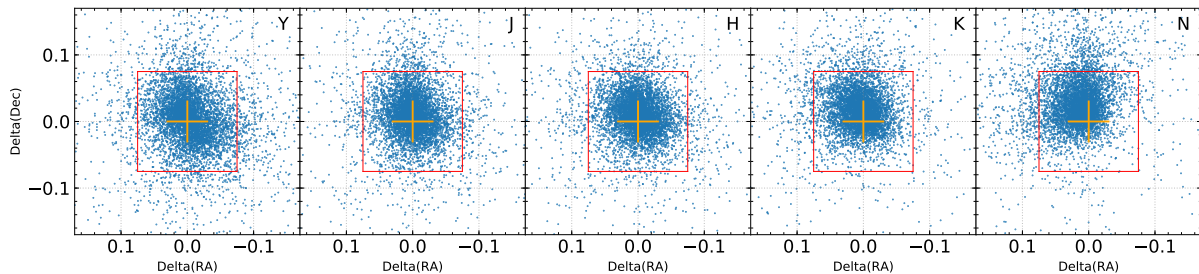


**Figure 5:** The distribution of measured vs. reference positions of the astrometric reference sources for all filters. The plot size is roughly one instrument pixel of 0.34 arcsec; in our stacks the pixel size is 0.15 arcsec. As mentioned in the text, the effect of proper motion between the UltraVISTA observations and the *Gaia* EDR3 epoch of 2016.0 has been ignored.

Filter	$\Delta\text{RA}$ [arcsec]		$\Delta\text{Dec}$ [arcsec]	
	mean	FWHM	mean	FWHM
<i>Y</i>	-0.005	0.117	0.004	0.130
<i>J</i>	-0.001	0.098	0.010	0.111
<i>H</i>	-0.001	0.099	0.010	0.098
<i>K<sub>s</sub></i>	0.006	0.095	0.017	0.094
NB118	0.016	0.107	0.029	0.112

**Table 2:** Overall astrometric accuracy, all filters, full stacks. As the effect of proper motion between the UltraVISTA observations and the *Gaia* EDR3 epoch of 2016.0 has been ignored (see text), the actual astrometric accuracy is better than listed here.

But since we are using a single catalogue whose epoch is 2016 to cover observations between end 2009 and early 2023, the larger the time difference between the observing epoch and the epoch of the reference catalogue, the larger the offset and the scatter. Note that this is because the measurement relies on the reference stars, which have their proper motions, while the objects of interest in this programme are rather the galaxies which do not move. This can also cause problems when stacking an object that has moved significantly as the code has to choose which position to privilege; but this affects only the high proper motion objects, namely the bright nearby stars.

To investigate the importance of the differing observing times, we built stacks for each season, and measured the astrometric accuracy separately for each season using the nominal EDR3 catalogue. This is shown in the top panel of Figure 6, which clearly shows a monotonic shift with time, and a dispersion decreasing from 2009 to 2016, and increasing thereafter. The bottom panel shows the result of the same exercise but using reference catalogues shifted to the mean epoch of observation of each season (namely the ones used in the determination of the astrometric solution of each individual file, as described in Section 4.1); here the monotonic shift with time has nearly vanished, and while there remains a slight modulation of the dispersion, it is very minor; the numerical values are reported in Table 3. The figure is shown for the *H* filter which has observations during all seasons; the other filters show the same effect, though with one or more empty panels.

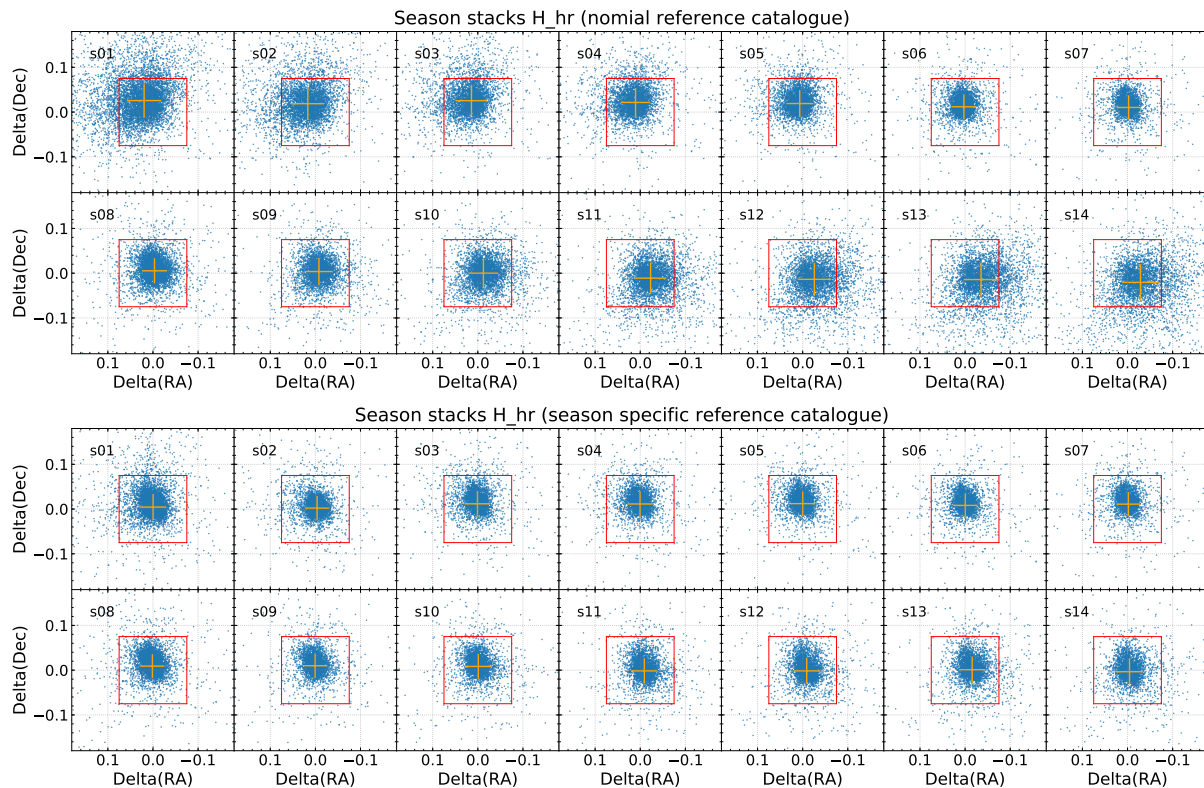


**Figure 6:** Astrometric accuracy in  $H$ -band single-season stacks, evaluated using a single reference catalogue with epoch 2016.0 (top) and with season-shifted (i.e. epoch matched) catalogues (bottom)

Season	#	Single reference file				Season reference files			
		$\Delta$ RA [arcsec]		$\Delta$ Dec [arcsec]		$\Delta$ RA [arcsec]		$\Delta$ Dec [arcsec]	
		mean	fwhm	mean	fwhm	mean	fwhm	mean	fwhm
2009–2010	1	−0.020	0.136	−0.026	0.132	0.000	0.079	−0.004	0.086
2010–2011	2	−0.017	0.124	−0.019	0.120	0.004	0.070	−0.002	0.071
2011–2012	3	−0.014	0.112	−0.025	0.107	−0.001	0.076	−0.012	0.078
2012–2013	4	−0.010	0.098	−0.021	0.094	−0.000	0.075	−0.011	0.075
2013–2014	5	−0.006	0.084	−0.019	0.085	0.000	0.071	−0.012	0.073
2014–2015	6	−0.003	0.072	−0.012	0.071	0.000	0.068	−0.008	0.069
2015–2016	7	0.002	0.067	−0.010	0.070	0.002	0.067	−0.011	0.070
2016–2017	8	0.003	0.073	−0.005	0.075	−0.001	0.066	−0.009	0.070
2017–2018	9	0.008	0.088	−0.004	0.086	−0.001	0.071	−0.010	0.072
2018–2019	10	0.012	0.102	−0.000	0.098	0.001	0.073	−0.008	0.075
2019–2020	11	0.023	0.114	0.011	0.112	0.009	0.074	0.002	0.079
2020–2021	12	0.026	0.129	0.014	0.124	0.009	0.077	0.002	0.083
2021–2022	13	0.035	0.139	0.014	0.129	0.016	0.080	−0.001	0.082
2022–2023	14	0.029	0.154	0.021	0.140	0.004	0.084	0.003	0.084

**Table 3:** Astrometry accuracy in  $H$ -band single-season stacks measured with single and season specific reference catalogues: mean and FWHM of the differences in RA and Dec when using the regular *Gaia* EDR3 catalogue (epoch 2016), and with the catalogues shifted to the mean epoch of the observations of each season.

To investigate the effect of using a single catalogue on a stack with sections (stripes/columns in our case) observed at different times, we plot the differences between the measured and the reference RA and Dec as a function of RA, see Figure 7, which clearly shows the column effects: (1) a different offset and (2) a different spread between the deep and ultra-deep columns. As can be seen in Figure 2 the ultra-deep columns were observed between seasons 1 and 8 for all filters, while the deep ones were observed earlier at  $K_s$  and very late at  $Y$ . As a consequence the effect is weakest at  $K_s$  and strongest at  $Y$  (excluding the NB118 case, where the effect is weak because of the few observations of the deep columns which were all obtained during season 1).

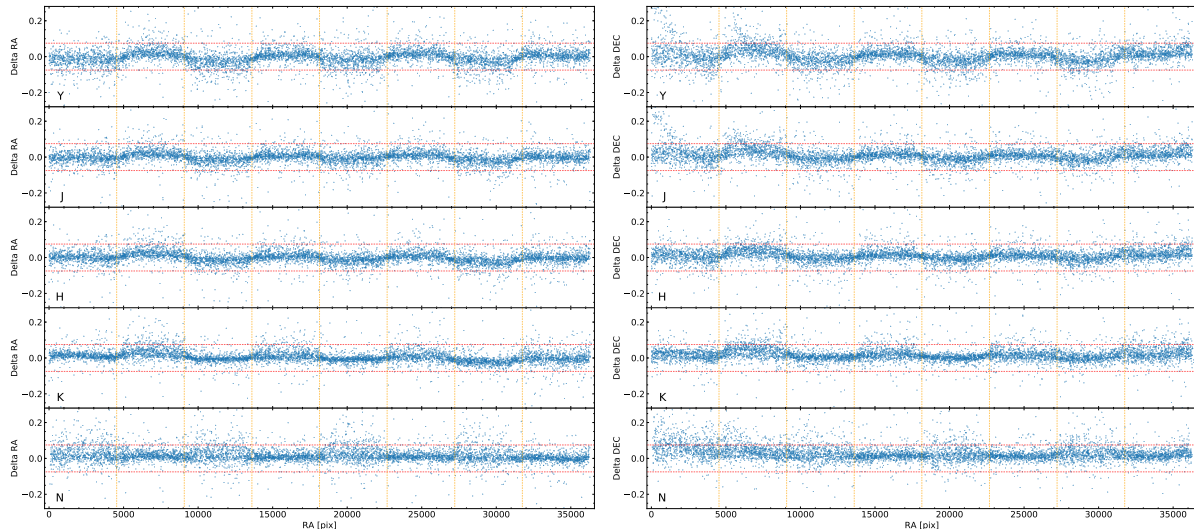


**Figure 7:** Measured RA and Dec offsets, in arcsec, vs. RA, in pixels, between observed and reference positions over the region observed. The red dotted horizontal lines span the size of a pixel in the final stacks. The variation is due to the use of a single reference catalogue while the mean dates of the observations differ between the ultra-deep and deep columns.

In conclusion, the overall astrometric accuracy,  $\sim 1/3$  of a stack pixel, is excellent. A more accurate, but filter and position-dependent evaluation, could be obtained by measuring separately the deep and ultra-deep columns and using specific catalogues shifted to the mean observing epoch of filter and column pair, listed in Table 4. But for the purposes of this document, the single, global value is deemed sufficient.

Filter	ultra-deep	deep	entire stack
$Y$	2013.85	2020.61	2017.35
$J$	2014.11	2018.71	2016.34
$H$	2013.84	2018.55	2016.09
$K_s$	2013.07	2016.99	2014.98
NB118	2014.48	2010.05	2014.10

**Table 4:** Mean epochs of the observations used to create the DR6 stacks in the 5 filters, broken down by set of stripes as well as for the entire stack. The mean is weighted by the exposure time of the individual images (only relevant for NB118, where the exposure time changed over the survey, see the caption to Fig. 2).

#### 4.4.2 Comparison of photometry between DR5 and DR6

We also compared the photometry of sources in the DR6 stacks with the previous DR5 stacks. Figure 8 shows the difference between `MAG_AUTO` magnitudes measured for all sources in DR5 and in DR6. The small points show one point in fifty. The large points show the median magnitude, and the red lines indicate the region covered by 68% of the points. In all cases, the difference in photometry is less than 0.01 magnitudes in the median. The Y band shows an asymmetric scatter that could be due to a difference in seeing in the deep stripes (where the exposure time increased a lot, from 9.9 h/px to 181.7 h/px) that the `MAG_AUTO` estimator may not perfectly correct for.

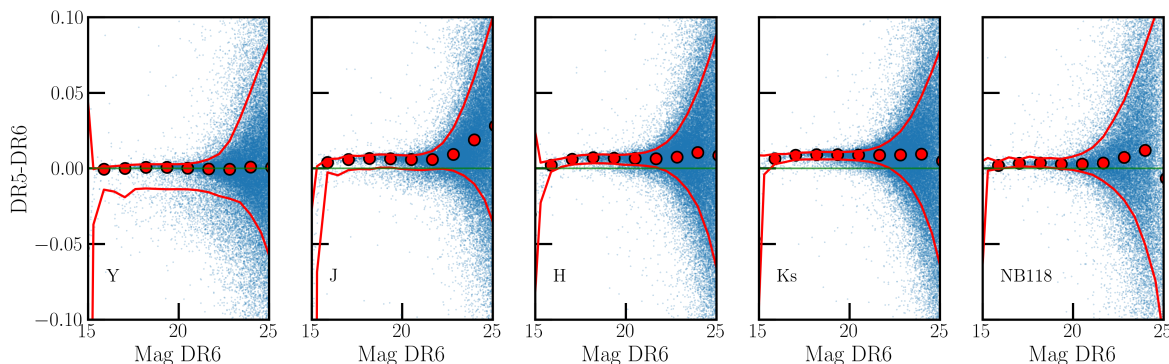


**Figure 8:** Difference in `MAG_AUTO` magnitudes for all sources measured in DR5 and DR6. The filled points show the median values and the solid lines indicate the region covered by 68% of the points.

#### 4.4.3 Sky noise and limiting magnitudes

The  $5\sigma$  noise in the stacks in  $2''$  apertures was computed using empty apertures (regions of the images which contained no pixels identified as objects).

We computed the noise in the two sets of stripes (deep and ultra-deep), and we also computed the noise in the DR4 and DR5 stacks in exactly the same way to track the change in depth. The results are given in Table 5 and in Figs. 9–13. These values represent the  $5\sigma$  noise in  $2''$  apertures — they do not include an aperture correction (of around 0.3 mag, see below) to total magnitude, and in that sense they are not limiting magnitudes. The two sets of stripes have a small overlap on the sky, but for computing the noise reported here we used sufficiently narrow (in RA) definitions of the stripes that this overlap is not used in the analysis. The table highlights three key features of DR6: (1) The depth in the Y band in the deep stripes has increased substantially (1.1 mag) with respect to DR5; (2) The depth in the four broad-band filters is essentially uniform over the full  $1.5^\circ \times 1.2^\circ$  UltraVISTA field (i.e. in the two sets of stripes); (3) The addition of the NB118 GTO data (Milvang-Jensen et al. 2013) to DR6 adds (somewhat shallow) coverage in the deep stripes.

For the Phase 3 headers, the limiting magnitude needs to be stated. We computed that by subtracting an approximate aperture correction (from  $2''$  to total magnitude) of 0.3 mag from the  $5\sigma$  noise values reported for DR6 in Tab. 5. These limiting magnitudes are listed in Tab. 6. Table 6 also lists the typical exposure times per pixel, in hours, for the two sets of stripes.

Filter	Stripes	DR4	DR5	DR6	DR5–DR4	DR6–DR5
<i>Y</i>	ultra-deep	26.01	26.02	25.95	0.01	−0.07
<i>Y</i>	deep	24.91	24.83	25.96	−0.08	1.13
<i>J</i>	ultra-deep	25.80	25.85	25.79	0.05	−0.06
<i>J</i>	deep	24.71	25.67	25.80	0.96	0.14
<i>H</i>	ultra-deep	25.48	25.48	25.47	0.00	−0.01
<i>H</i>	deep	24.38	25.34	25.48	0.96	0.14
<i>K<sub>s</sub></i>	ultra-deep	25.12	25.14	25.12	0.02	−0.02
<i>K<sub>s</sub></i>	deep	24.77	25.00	25.07	0.23	0.06
NB118	ultra-deep	24.54	24.64	24.64	0.10	0.00
NB118	deep	...	...	23.52	...	...

**Table 5:** The  $5\sigma$  noise in  $2''$  apertures in AB mag in DR4 and DR5 (for reference) and in DR6, computed in the same way. The final two columns give the change in noise (and hence change in depth or limiting magnitude).

These values are calculated as the total time spent on the given set of stripes, multiplied by  $2/3$ , reflecting that a typical point (pixel) on the sky will be covered by 2 of the 3 pawprints that make up a given set of stripes (this is due to the gaps between the detectors of VIRCAM). The PSF FWHM and ellipticity in the stacks (not split by stripes) were measured using PSFEx, and are also listed in Tab. 6.

Filter	Exposure time per px [hrs]		Limiting mag. $5\sigma, 2''$ [AB mag]		FWHM [arcsec]	Ellipticity
	Ultra-deep	Deep	Ultra-deep	Deep	Entire image	Entire image
<i>Y</i>	169.5	181.7	25.7	25.7	0.78	0.01
<i>J</i>	176.7	166.8	25.5	25.5	0.77	0.01
<i>H</i>	191.7	175.1	25.2	25.2	0.76	0.01
<i>K<sub>s</sub></i>	171.4	163.4	24.8	24.8	0.76	0.01
NB118	119.4	11.0	24.3	23.2	0.77	0.01

**Table 6:** Characteristics of the images: typical exposure time per pixel and limiting magnitudes in both deep and ultra-deep regions and PSF FWHM and ellipticity measured in the entire image. **Important note:** The  $5\sigma$  limiting magnitudes listed in this table and in the headers are computed using “empty aperture” measurements in  $2.0''$  diameter apertures, and are subsequently corrected to total magnitude by subtracting 0.3 mag. This is the same procedure used for DR5.

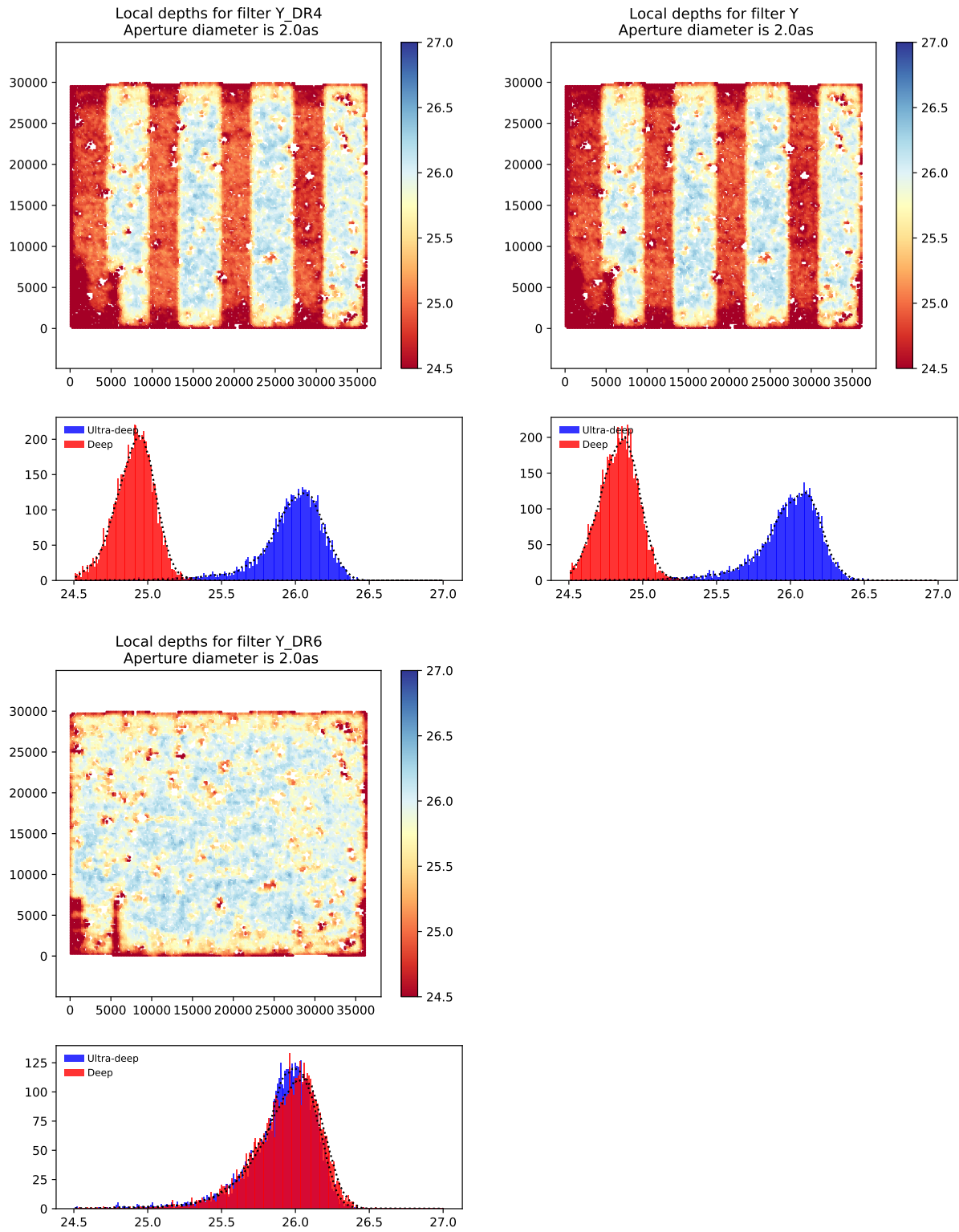


**Figure 9:** Y-band empty aperture noise measurements. The map shows the  $5\sigma$  noise in  $2''$  apertures in AB mag over the  $1.5^\circ \times 1.2^\circ$  UltraVISTA field, and the histogram shows the same quantity split into the two sets of stripes (ultra-deep and deep). **Top left:** DR4, **top right:** DR5, **bottom:** DR6.

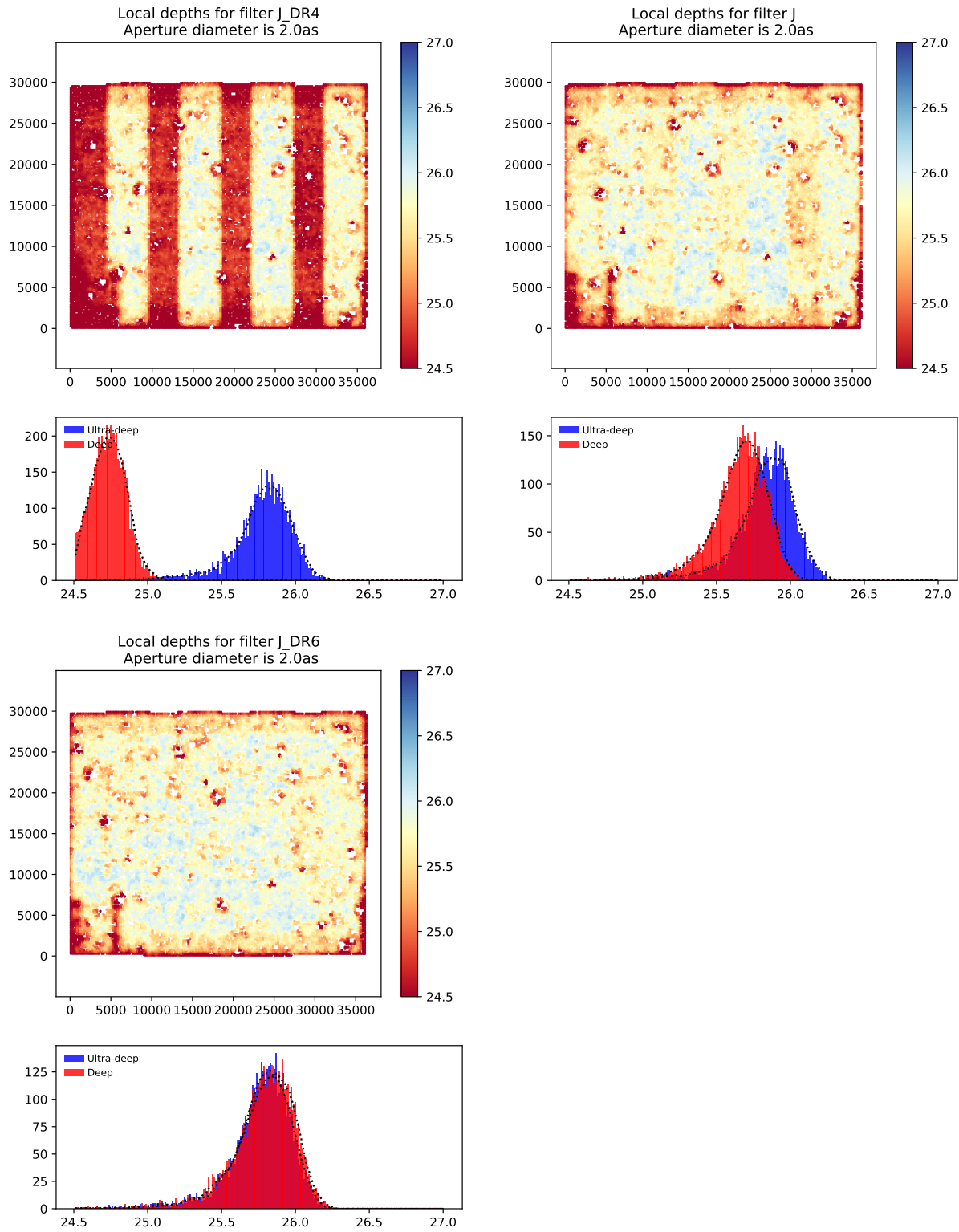


**Figure 10:** *J*-band empty aperture noise measurements. The map shows the  $5\sigma$  noise in  $2''$  apertures in AB mag over the  $1.5^\circ \times 1.2^\circ$  UltraVISTA field, and the histogram shows the same quantity split into the two sets of stripes (ultra-deep and deep). **Top left:** DR4, **top right:** DR5, **bottom:** DR6.



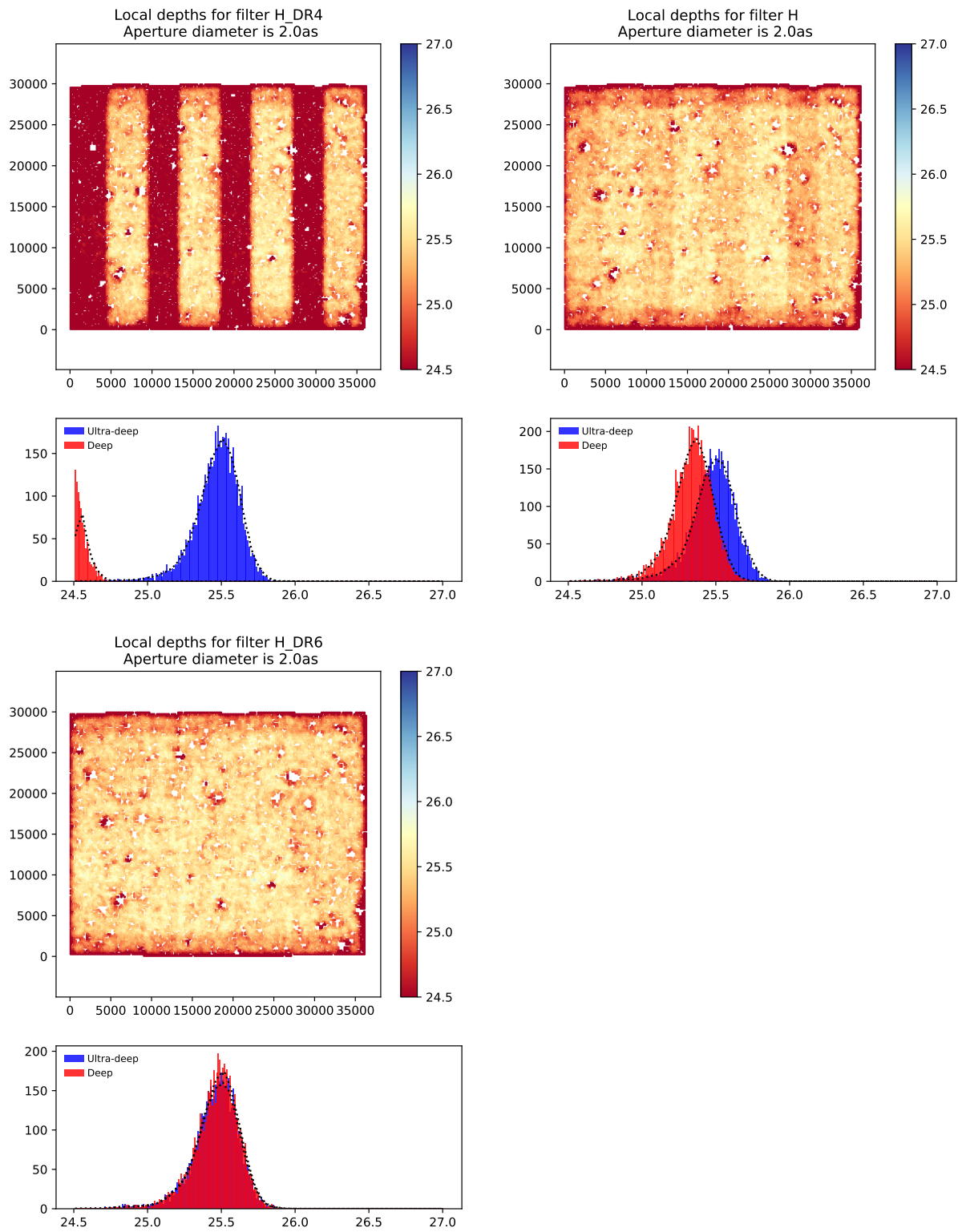


**Figure 11:** *H*-band empty aperture noise measurements. The map shows the  $5\sigma$  noise in  $2''$  apertures in AB mag over the  $1.5^\circ \times 1.2^\circ$  UltraVISTA field, and the histogram shows the same quantity split into the two sets of stripes (ultra-deep and deep). **Top left:** DR4, **top right:** DR5, **bottom:** DR6.

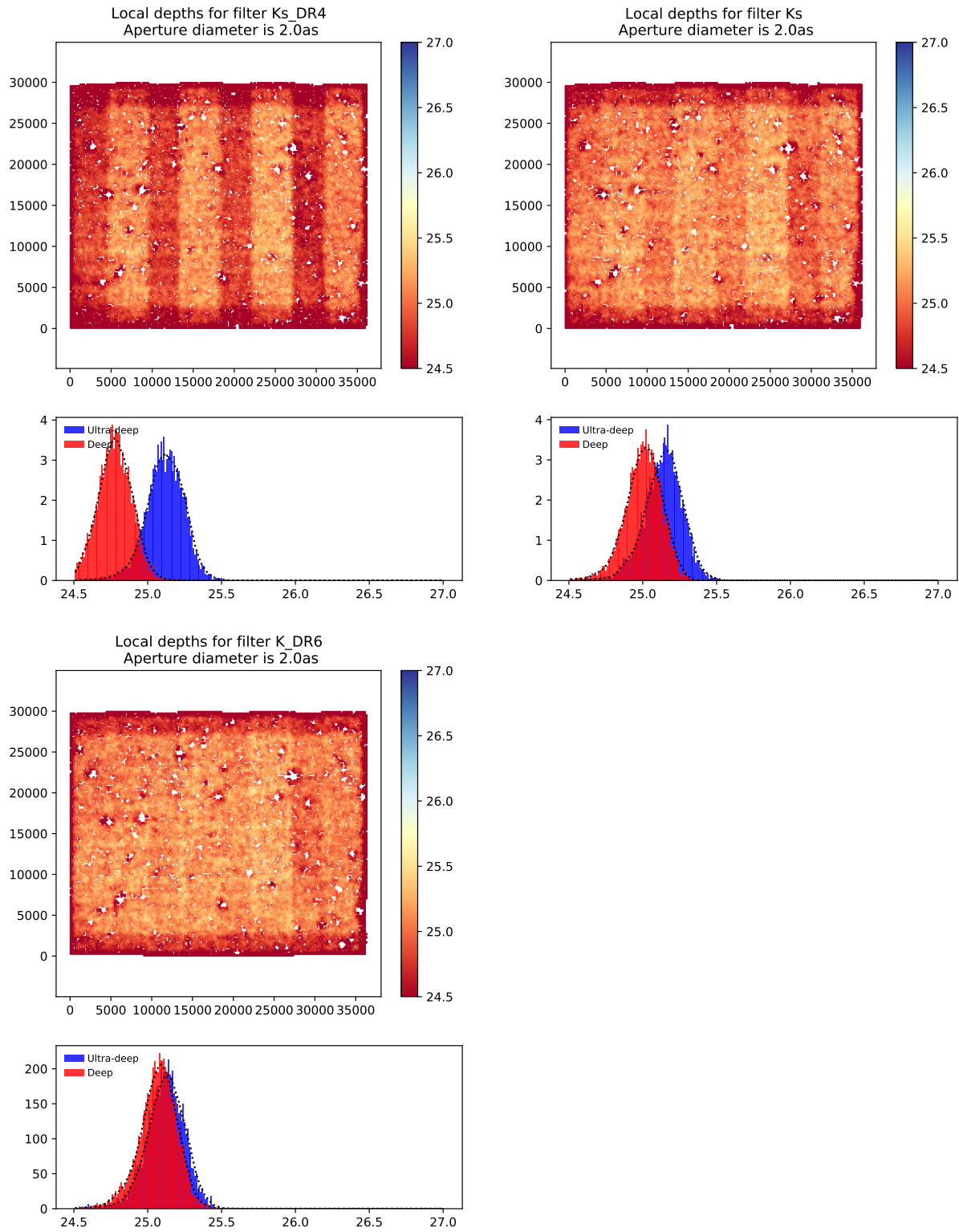


**Figure 12:**  $K_s$ -band empty aperture noise measurements. The map shows the  $5\sigma$  noise in  $2''$  apertures in AB mag over the  $1.5^\circ \times 1.2^\circ$  UltraVISTA field, and the histogram shows the same quantity split into the two sets of stripes (ultra-deep and deep). **Top left:** DR4, **top right:** DR5, **bottom:** DR6.

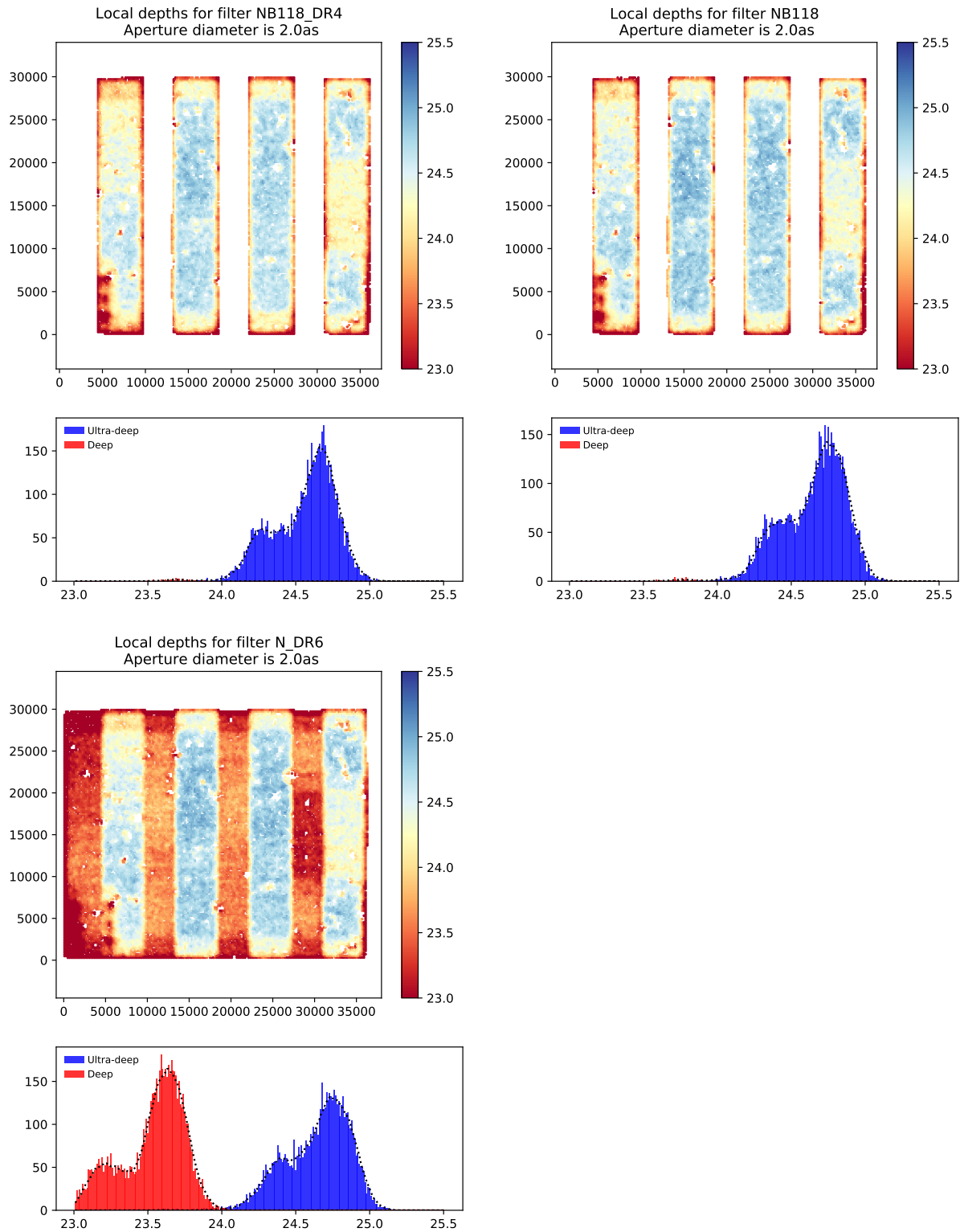


**Figure 13:** NB118 empty aperture noise measurements. The map shows the  $5\sigma$  noise in  $2''$  apertures in AB mag over the  $1.5^\circ \times 1.2^\circ$  UltraVISTA field, and the histogram shows the same quantity split into the two sets of stripes (ultra-deep and deep). **Top left:** DR4, **top right:** DR5, **bottom:** DR6.

#### 4.4.4 Noise behaviour

Here we use the pipeline final stacks and other intermediate stacks to investigate how the sky background noise varies with increasing integration time. To measure the sky noise we begin by finding a set of empty apertures valid for all stacks and thus all filters: a `SExtractor` segmentation map is produced for each final stack, the five maps are added to produce a single global one. Next a coordinate pair is chosen randomly, but excluding the edges of the observed region, which have low coverage and are noisy. The sum of the pixel values in a box (aperture) of  $6'' = 40$  pix is computed and if null those coordinates are retained in a ds9 region file, and the aperture is filled with 9's in order to avoid it in the future. Note that the box size is much larger than the  $2''$  used in the empty aperture measurements above, and this is done explicitly to maintain an extra margin away from the wings of sources. The procedure is repeated 1,000,000 times, which yields  $\sim 77,000$  empty apertures. One minor problem is that the segmentation system fails around the very brightest stars with extensive reflection rings around them: there are extensive regions covered by the reflection rings that are left as blank, thus leaving a few 10's of empty apertures there. These will have to be removed later by excluding apertures with fluxes clearly significant.

We then measure the flux (sum of the pixel values) and the noise (width of the flux distribution, using `MAD_std`) in 35,000 boxes of side 14 pix ( $2.1''$ ) centred on the empty apertures found and on various stacks of data from a single paw and with different integration times, namely:

1. pipeline substacks (intermediate products, all single paw by construction),
2. pipeline paw stacks (combinations of the above)
3. ad-hoc stacks of 4, 8, 16, ... 1024 files in each paw, working forward from the beginning and working backward from the end of the mission, thus giving 9 measurements in each case,
4. ad-hoc stacks of 2, 3, 4, ... pipeline substacks, the last one being the paw stack.

Note that items 1 and 3 are built by combining (`Swarping`) files, while items 2 and 4 are built by combining previously built stacks, and this gives us a chance to demonstrate the the two procedures give the same result (4.3).

For each stack the integration time is computed as the total  $N \times \text{DIT}$  of all the files combined to built it, where DIT is the actual integration time, and  $N$  is the number of frames combined during acquisition at the instrument level. Figure 14 shows the measured noise in the box aperture vs. the square root of the integration time. The stacks built from files are plotted in blue, the ones built from stacks are shows in orange. The NB118 data, not shown, shows the same behaviour.

The apparently large vertical dispersion of the noise for the stacks with short integration times is normal since the observations were not obtained in the same conditions mostly due to the variation in the sky background. A selection of different groups of 4, 8, or 16 files would have given different results.

A straight line is fit to the data up to 2.3 in the abscissa, and the slope is reported in the figures. In optimal conditions it should be 1.0, and here we see that it is very close to that value. The value of 2.3 was chosen arbitrarily; fitting the data up to values  $< 2.3$  will produce a steeper slope, and vice-versa for fits to larger values. In fact it is clear that at values  $> 2.4$  the data deviate from the optimal straight line. The exact reason for this has not been investigated.

It is important to note that there is a region of overlap of the two types of stacks, which supports

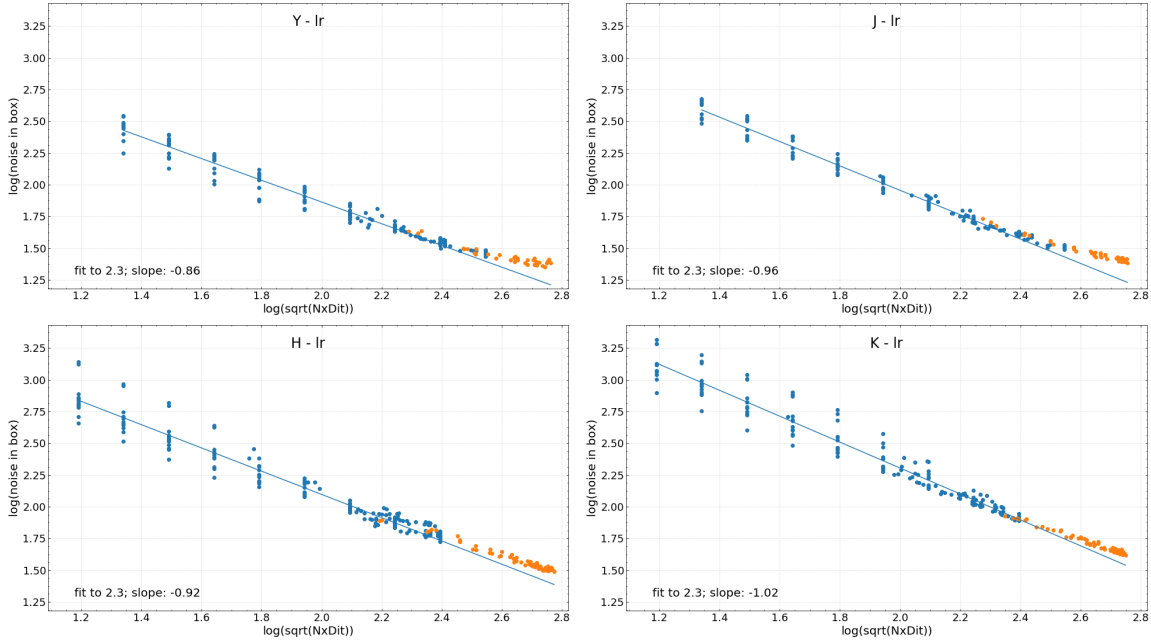


**Figure 14:** Noise in box aperture vs. square root of the integration time. In blue stacks built from files, and in orange stacks built from other stacks.

the assumption that **Swarping** files in groups into substacks and then combining the substacks produces the same results and combining all the files into the final stack in a single run.

## 4.5 Previous releases

The science files in DR6 (stacks, sources lists and the 5-band catalogue) supersede – or in the Phase 3 terminology: *update* – the corresponding science files from DR5, which in turn did the same for those in DR4, etc.

The “DR4.1” and “DR4.1.1” releases, which is the Weaver et al. (2022) COSMOS2020 multi-band (ca. 40 bands) catalogues based on the UltraVISTA DR4 images and other data (UV, optical, IR, ...), are not “superseded” (updated) by this DR6 release, as it does not contain such  $\sim 40$ -band catalogues (only a 5-band catalogue based on the UltraVISTA data alone). For information: DR4.1 was the initial release of the two COSMOS2020 catalogues, called Classic and Farmer. DR4.1.1 contains an updated version of the Farmer catalogue where a minor error has been corrected.

## 4.6 Software versions

DR6 makes extensive use of the **Astromatic**<sup>7</sup> software. A complete list of software versions used is listed in Table 7.

<sup>7</sup><https://www.astromatic.net/>

Software name	Version
SExtractor	2.24.2
PSFEx	3.22.1
Scamp	2.10.0
SWarp	2.41.5
WeightWatcher	1.12
MissFITS	2.8.0

**Table 7:** Software versions used in UltraVISTA DR6.

## 5 Data format

### 5.1 File types

All images and catalogues are distributed in FITS format. In this release, we provide five stacked images and their corresponding weight maps for  $Y$ ,  $J$ ,  $H$ ,  $K_s$ , and NB118 narrow-band data composed of images from all 14 years of the UltraVISTA survey plus data from the NB118 GTO run (Milvang-Jensen et al. 2013). The various ESO programmes used to make DR6 are listed in Tab. 1.

Given the deep and ultra-deep sections have different exposure times (although only by a small factor in the four broad-band stacks, cf. Tab. 6), this has the consequence that the signal-to-noise ratio for an object of a given magnitude will vary across the image. An inspection of the weight map provided with each image will indicate the location of the deeper zones.

Images have a zero-point of 30.0 AB magnitudes for a one second equivalent exposure time. The images have a pixel scale of  $0.15''/\text{pixel}$  and have the same pixel grid (number of pixels and tangent point) as the other publicly available IRSA/COSMOS images. Each image is  $\sim 9$  GB in size.

Following the ESO Phase 3 standard, the FITS files for the 5 stacks are multi-extension FITS files, with the stacked image in the primary HDU (header data unit) and with a “provenance table” in the first (and only) extension. The provenance table lists all the raw images that (after processing at CASU and CANDIDE/CALET) were combined to make the given stack. The provenance table for an image stack applies also to its weight map and is not repeated there.

### 5.2 Complete list of distributed products

Tables 8 and 9 list the imaging, source list and catalogue data products distributed in DR6. Five images are provided, as well as their corresponding weight maps. These weight-maps correspond to the MAP\_WEIGHT images produced by **Swarp** and have pixel values proportional to the inverse variance. We note that we plan to put all the 20 DR6 files on our website<sup>8</sup>.

We provide two source lists for each band: a “dual-image mode” list, in which the  $K_s$  image is used for source detection and the band image is used as the measurement (i.e., the measurement is done at the position of the source in the  $K_s$  band); and a “single-image mode” list in which the image is used for both detection and measurement. Dual-image mode source lists have the

---

<sup>8</sup><http://www.ultravista.org/>

Filename	Description
UVISTA_Y_12_01_24_allpaw_skysub_015_dr6_rc_v1.fits	Y-band stack
UVISTA_Y_12_01_24_allpaw_skysub_015_dr6_rc_v1.weight.fits	Y-band weight
UVISTA_J_12_01_24_allpaw_skysub_015_dr6_rc_v1.fits	J-band stack
UVISTA_J_12_01_24_allpaw_skysub_015_dr6_rc_v1.weight.fits	J-band weight
UVISTA_H_12_01_24_allpaw_skysub_015_dr6_rc_v1.fits	H-band stack
UVISTA_H_12_01_24_allpaw_skysub_015_dr6_rc_v1.weight.fits	H-band weight
UVISTA_Ks_12_01_24_allpaw_skysub_015_dr6_rc_v1.fits	$K_s$ -band stack
UVISTA_Ks_12_01_24_allpaw_skysub_015_dr6_rc_v1.weight.fits	$K_s$ -band weight
UVISTA_NB118_12_01_24_allpaw_skysub_015_dr6_rc_v1.fits	NB118 stack
UVISTA_NB118_12_01_24_allpaw_skysub_015_dr6_rc_v1.weight.fits	NB118 weight

**Table 8:** Summary of DR6 stacked images and associated weight maps. All images have a zero point of 30.0 AB magnitudes for a one second equivalent exposure time and a scale of  $0.15''/\text{pixel}$ .

Filename	Detection	Measurement
UVISTA_Y_12_01_24_allpaw_skysub_015_dr6_rc_v1.cat.fits	Y	Y
UVISTA_J_12_01_24_allpaw_skysub_015_dr6_rc_v1.cat.fits	J	J
UVISTA_H_12_01_24_allpaw_skysub_015_dr6_rc_v1.cat.fits	H	H
UVISTA_Ks_12_01_24_allpaw_skysub_015_dr6_rc_v1.cat.fits	$K_s$	$K_s$
UVISTA_NB118_12_01_24_allpaw_skysub_015_dr6_rc_v1.cat.fits	NB118	NB118
UVISTA_Ks_12_01_24_allpaw_skysub_015_dr6_rc_v1_Y.cat.fits	$K_s$	Y
UVISTA_Ks_12_01_24_allpaw_skysub_015_dr6_rc_v1_J.cat.fits	$K_s$	J
UVISTA_Ks_12_01_24_allpaw_skysub_015_dr6_rc_v1_H.cat.fits	$K_s$	H
UVISTA_Ks_12_01_24_allpaw_skysub_015_dr6_rc_v1_NB118.cat.fits	$K_s$	NB118
UVISTA_5band_cat_dr6_rc_v1.fits	$K_s$	YJHK $_s$ NB118

**Table 9:** Source lists and catalogue products delivered with DR6.

advantage that, as the same number of entries is present in all source lists, colours can be easily computed for each object. On the other hand, the single-image mode lists contain, in principle, all sources to a given detection threshold ( $1.8\sigma$ ). Source lists were extracted using `SExtractor` (Bertin & Arnouts 1996) version 2.28.2 compiled and downloaded from the `astromatic.net`<sup>9</sup>. For each entry in the source list we provide flux measurements in 18 photometric apertures. Their diameters in pixels ( $1 \text{ px} = 0.15''$ ) are as follows, corresponding to three apertures of  $2''$ ,  $3''$  and  $7.1''$  and logarithmically spaced apertures from  $0.5''$  to  $5''$ :

13.33, 20.00, 47.33,  
3.33, 3.93, 4.63, 5.46, 6.44, 7.59, 8.94, 10.54, 12.43, 14.65, 17.26, 20.35, 23.99, 28.28, 33.33

We also provide a 5-band catalogue `UVISTA_5band_cat_dr6_rc_v1.fits` created from the five  $K_s$ -selected source lists. The columns in this catalogue are described in Tab. 10. Two additional columns are provided: the  $E(B-V)$  Galactic reddening measured at the position of each object in the Schlegel et al. (1998) dust maps, and a flag which indicates the field border.

<sup>9</sup><http://astromatic.net/software/sextractor>

Column no.	Column name	Description
1	SOURCE_ID	UltraVISTA source designation, e.g. UVISTADR6 J100018.61+013540.3
2	NUMBER	Running object number
3	ALPHA_J2000	Right ascension of barycenter in decimal degrees (J2000)
4	DELTA_J2000	Declination of barycenter in decimal degrees (J2000)
5	X_IMAGE	Object position along x
6	Y_IMAGE	Object position along y
7	FLAG_HJMCC	Bad region flag: != 0 for bad region (field boundaries: 1)
8	EBV	Galactic reddening E(B-V) based on Schlegel et al (1998) dust maps
9	Y_APER2	Y fixed aperture magnitude (2'' diameter)
10	Y_APER2_ERR	Y fixed aperture mag error (2'' diameter)
11	Y_APER7	Y fixed aperture magnitude (7.1'' diameter)
12	Y_APER7_ERR	Y fixed aperture mag error (7.1'' diameter)
13	Y_AUTO	Y auto magnitude
14	Y_AUTO_ERR	Y auto mag error
15	Y_FLUX_RADIUS	Radius of aperture containing half the flux of Y_AUTO
16	Y_FLAG	Y Flag (SExtractor)
17	J_APER2	J fixed aperture magnitude (2'' diameter)
18	J_APER2_ERR	J fixed aperture mag error (2'' diameter)
19	J_APER7	J fixed aperture magnitude (7.1'' diameter)
20	J_APER7_ERR	J fixed aperture mag error (7.1'' diameter)
21	J_AUTO	J auto magnitude
22	J_AUTO_ERR	J auto mag error
23	J_FLUX_RADIUS	Radius of aperture containing half the flux of J_AUTO
24	J_FLAG	J Flag (SExtractor)
25	H_APER2	H fixed aperture magnitude (2'' diameter)
26	H_APER2_ERR	H fixed aperture mag error (2'' diameter)
27	H_APER7	H fixed aperture magnitude (7.1'' diameter)
28	H_APER7_ERR	H fixed aperture mag error (7.1'' diameter)
29	H_AUTO	H auto magnitude
30	H_AUTO_ERR	H auto mag error
31	H_FLUX_RADIUS	Radius of aperture containing half the flux of H_AUTO
32	H_FLAG	H Flag (SExtractor)
33	KS_APER2	Ks fixed aperture magnitude (2'' diameter) [detection image]
34	KS_APER2_ERR	Ks fixed aperture mag error (2'' diameter) [detection image]
35	KS_APER7	Ks fixed aperture magnitude (7.1'' diameter) [detection image]
36	KS_APER7_ERR	Ks fixed aperture mag error (7.1'' diameter) [detection image]
37	KS_AUTO	Ks auto magnitude [detection image]
38	KS_AUTO_ERR	Ks auto mag error [detection image]
39	KS_FLUX_RADIUS	Radius of aperture containing half the flux of KS_AUTO
40	KS_FLAG	Ks Flag (SExtractor) [detection image]
41	NB118_APER2	NB118 fixed aperture magnitude (2'' diameter)
42	NB118_APER2_ERR	NB118 fixed aperture mag error (2'' diameter)
43	NB118_APER7	NB118 fixed aperture magnitude (7.1'' diameter)
44	NB118_APER7_ERR	NB118 fixed aperture mag error (7.1'' diameter)
45	NB118_AUTO	NB118 auto magnitude
46	NB118_AUTO_ERR	NB118 auto mag error
47	NB118_FLUX_RADIUS	Radius of aperture containing half the flux of NB118_AUTO
48	NB118_FLAG	NB118 Flag (SExtractor)

**Table 10:** List of columns in the five-band merged catalogue. All magnitudes are in the AB system.



## 6 Release of the CASU single OB pawprint stacks at VSA/WFAU

As part of the VISTA Data Flow System (e.g. Emerson et al. 2004), CASU produces stacks of the data contained in a single OB and on a single pawprint (e.g. Irwin et al. 2004; Lewis et al. 2010, and the CASU web site<sup>10</sup>). These stacks have `_st` in the file names and are sometimes called `_st` stacks. The UltraVISTA OBs typically comprise 0.5 or 1 hour exposure on a given pawprint, and in UltraVISTA we have somewhat imprecisely referred to these CASU stacks as the “1-hour stacks”. Throughout the UltraVISTA program we have supplied these stacks to interested parties on a best-effort basis. To make these data more widely available we are, since DR4, releasing these stacks through the VISTA Science Archive (VSA, e.g. Hambly et al. 2004; Cross et al. 2012) at the Wide Field Astronomy Unit (WFAU) at Edinburgh, concurrent with the ESO data release of our deep stacks.

It should be noted that our deep stacks are made by redoing the sky subtraction of the individual images corresponding to 1 or 2 minutes of exposure and then stacking these; our deep stacks are not made by stacking the CASU `_st` stacks. We have not used the CASU stacks in our processing, and we are providing them via the VSA “as is”.

The VSA will not only allow the user to download selected or all of the CASU stacks and their confidence maps, it will also allow the user to upload a text file with coordinates of one or more objects, and then in a second step get the photometry from each CASU stack, giving a table including aperture-corrected magnitude and time (MJDOBS), from which a light curve in the five UltraVISTA bands can be plotted.

### 6.1 The CASU single OB pawprint stacks at the VSA

#### 6.1.1 Cookbook: How to download the CASU single OB pawprint stacks and their confidence maps

Go to the VSA (VISTA Science Archive) home page <http://surveys.roe.ac.uk/vsa>

There is no need to login

Click “Archive Listing”

Under “Select the programme/survey you wish to use:” select “UltraVISTA”

Under “Database release to use:” select “ULTRAVISTADR6”

Under “Observation type:” leave it at “object”

Under “Frame type:” select “stack (pawprint)”

Possibly limit by filter or time period

Possibly increase “Rows per page:” up to a max of 1000

Click GetList

Then download the CASU single OB pawprint stacks via the “Link to image wget script” link

To get the CASU confidence maps for these stacks, in the form do:

Under “Observation type:” select “confidence”

Under “Frame type:” select “stack (pawprint)” (as before)

---

<sup>10</sup><http://casu.ast.cam.ac.uk/surveys-projects/vista/technical/data-processing>

## 7 Acknowledgements

We acknowledge the vital contribution of Olivier Le Fèvre to the UltraVISTA project. Olivier helped design the survey and was one of the four original PIs of the project. His untimely death in 2020 meant that he did not see the completion of the survey that he helped to start.

This UltraVISTA release has been made possible thanks to a significant infrastructure grant from “Domaine d’intérêt majeur en astrophysique et conditions d’apparition de la vie (DIM-ACAV+)”. HJMCC acknowledges financial support from the “Programme national cosmologie et galaxies” (PNCG). JSD acknowledges the support of the UK Science and Technology Facilities Council (STFC) and the support of the Royal Society through a Research Professorship. The Cosmic Dawn Center (DAWN) is funded by the Danish National Research Foundation under grant DNR140. The UltraVISTA team would like to thank the ESO staff for scheduling and making the UltraVISTA observations. We thank E. Bertin for many useful discussions concerning the usage of the *Astromatic* tool set. This research has made use of the *VizieR* catalogue access tool provided by the CDS, Strasbourg, France. This work has made use of data from the European Space Agency (ESA) mission *Gaia* (<https://www.cosmos.esa.int/gaia>), processed by the *Gaia* Data Processing and Analysis Consortium (DPAC, <https://www.cosmos.esa.int/web/gaia/dpac/consortium>). Funding for the DPAC has been provided by national institutions, in particular the institutions participating in the *Gaia* Multilateral Agreement.

## References

- Bertin, E. 2011, in *Astronomical Society of the Pacific Conference Series*, Vol. 442, *Astronomical Data Analysis Software and Systems XX*, ed. I. N. Evans, A. Accomazzi, D. J. Mink, & A. H. Rots, 435
- Bertin, E. & Arnouts, S. 1996, *ApJS*, 117, 393
- Bertin, E., Mellier, Y., Radovich, M., et al. 2002, in *Astronomical Society of the Pacific Conference Series*, Vol. 281, *Astronomical Data Analysis Software and Systems XI*, ed. D. A. Bohlender, D. Durand, & T. H. Handley, 228
- Cross, N. J. G., Collins, R. S., Mann, R. G., et al. 2012, *A&A*, 548, A119
- Dunlop, J. S., Bowler, R. A. A., Franx, M., et al. 2023, in *A Decade of ESO Wide-field Imaging Surveys*, 10 (<https://doi.org/10.5281/zenodo.10150386> or <https://ui.adsabs.harvard.edu/abs/2023dewi.confE..10D/abstract>)
- Emerson, J. P., Irwin, M. J., Lewis, J., et al. 2004, in *Society of Photo-Optical Instrumentation Engineers (SPIE) Conference Series*, Vol. 5493, *Society of Photo-Optical Instrumentation Engineers (SPIE) Conference Series*, ed. P. J. Quinn & A. Bridger, 401–410
- Gaia* Collaboration, Brown, A. G. A., Vallenari, A., et al. 2021, *A&A*, 649, A1
- Gaia* Collaboration, Prusti, T., de Bruijne, J. H. J., et al. 2016, *A&A*, 595, A1
- Gruen, D., Seitz, S., & Bernstein, G. M. 2014, *Publications of the Astronomical Society of the Pacific*, 126, 158

- Hambly, N. C., Mann, R. G., Bond, I., et al. 2004, in Society of Photo-Optical Instrumentation Engineers (SPIE) Conference Series, Vol. 5493, Society of Photo-Optical Instrumentation Engineers (SPIE) Conference Series, ed. P. J. Quinn & A. Bridger, 423–431
- Irwin, M. J., Lewis, J., Hodgkin, S., et al. 2004, in Society of Photo-Optical Instrumentation Engineers (SPIE) Conference Series, Vol. 5493, Society of Photo-Optical Instrumentation Engineers (SPIE) Conference Series, ed. P. J. Quinn & A. Bridger, 411–422
- Lewis, J. R., Irwin, M., & Bunclark, P. 2010, in Astronomical Society of the Pacific Conference Series, Vol. 434, Astronomical Data Analysis Software and Systems XIX, ed. Y. Mizumoto, K.-I. Morita, & M. Ohishi, 91
- Lindgren, L., Klioner, S. A., Hernández, J., et al. 2021, *A&A*, 649, A2
- McCracken, H. J., Milvang-Jensen, B., Dunlop, J., et al. 2012, *A&A*, 544, A156
- Milvang-Jensen, B., Freudling, W., Zabl, J., et al. 2013, *A&A*, 560, A94
- Schlegel, D. J., Finkbeiner, D. P., & Davis, M. 1998, *ApJ*, 500, 525
- Scoville, N., Aussel, H., Brusa, M., et al. 2007, *ApJS*, 172, 1
- Weaver, J. R., Kauffmann, O. B., Ilbert, O., et al. 2022, *ApJS*, 258, 11